Monthly Notices
of the
ROYAL ASTRONOMICAL SOCIETY

MNRAS **462,** 2266–2274 (2016) doi:10.1093/mnras/stw1666

Optical and near-infrared polarimetric study of the RCW121 Galactic H II region

J. C. Serón Navarrete,[1,2★] A. Roman-Lopes,[1] Fabio. P. Santos,[3] G. A. P. Franco[4] and W. Reis[5]

[1]*Departamento de Física y Astronomía, Universidad de La Serena, Cisternas 1200, La Serena, Chile*
[2]*Cerro Tololo InterAmerican Observatory, Casilla 603, La Serena, Chile*
[3]*Center for Interdisciplinary Exploration and Research in Astrophysics (CIERA) and Department of Physics & Astronomy, Northwestern University, 2145 Sheridan Road, Evanston, IL 60208, USA*
[4]*Departamento de Física–ICEx–UFMG, Caixa Postal 702, 30.123-970 Belo Horizonte, Brazil*
[5]*Faculdade IBMEC–MG, 300 Rio Grande do Norte street, Belo Horizote MG, Brazil*

Accepted 2016 July 8. Received 2016 May 26; in original form 2015 November 3

ABSTRACT

We present a polarimetric study of the RCW121 star-forming region to derive the orientation of the sky-projected magnetic field component traced by the polarization vectors, the morphology of which tends to follow the cloud's structure. Individual polarization-angle values are consistent across the different bands, having a broad distribution towards the RCW121 H II region. We estimate the corresponding magnetic field orientation in the H II region to have a mean value of $-12^\circ \pm 7^\circ$. RCW121 shows an elongated shape in the same direction as the magnetic field orientation, which may be evidence that magnetic pressure opposes the H II region expansion. Serkowski's relation was used to determine individual values of the total-to-selective extinction ratio (R_V) distribution and a weighted mean value of $R_V = 3.17 \pm 0.05$. We derive a foreground component of the polarization degree that is consistent with the literature value for this Galactic region.

Key words: techniques: polarimetric – stars: formation – dust, extinction – H II regions – ISM: individual objects: RCW121 – ISM: magnetic fields.

1 INTRODUCTION

It is well known that stars form in molecular clouds and the main actors in this process are probably gravity, pressure, outflows, turbulence and magnetic fields (McKee & Ostriker 2007). However, the specific role each one plays is still being unveiled. Measurement of the polarization of starlight is a powerful tool to study the plane-of-sky component of the magnetic field. Polarimetric studies of H II regions allow us to understand how massive star formation impacts on the surrounding interstellar medium (ISM) and magnetic field lines. Interstellar dust grains polarize the background starlight, because of its anisotropy in light absorption (dichroism) and tendency to align (which means that this type of dust grain is not spherical) with the Galactic magnetic field. Recent observations and theory point to radiative alignment torques (RAT, proposed by Dolginov & Mytrophanov 1976) as the mechanism that best explains interstellar dust grain alignment (see Andersson, Lazarian & Vaillancourt 2015 for a review on dust alignment theory). Multiband measurements of polarization degree allow us to infer information about the grain size, as well as the total-to-selective extinction (R_V), using the empirical Serkowski's law (Serkowski, Mathewson & Ford 1975).

RCW121 (Rodgers, Campbell & Whiteoak 1960), also known as Sharpless 2-4 (Sharpless 1959), is located in the Galactic plane in the direction of Scorpio at an approximate heliocentric distance of 2 kpc (Tapia et al. 2014). It is a compact H II region of 1 arcmin angular diameter, probably associated with RCW122, positioned within a giant molecular cloud detected in CO (Arnal, Duronea & Testori 2009). H_2O(Sánchez-Monge et al. 2013) and methanol (Walsh et al. 1997) maser sources were also detected, as well as intense CS (2–1) emission (Bronfman, Nyman & May 1996). Additionally, a young stellar cluster embedded in this giant molecular complex was previously studied by Roman-Lopes & Abraham (2006) using near-infrared photometric data. The authors reported 96 candidates for cluster membership, 30 per cent of them presenting a near-infrared excess, probably due to the presence of discs and/or circumstellar dust. From the cluster colour–colour diagram, they identified the main ionizing source of the H II region, assigning it a spectral type O5V–O6V, deriving a mean visual extinction of $A_V = 5.49 \pm^{2.06}_{1.32}$ mag, a value computed by comparing the Bracket gamma and 5-GHz flux densities. For the associated H II region, the authors determined emission measure and electronic density values

★ E-mail: jseron@dfuls.cl

Table 1. The polarimetric data used in this work were taken at Cerro Tololo InterAmerican Observatory (CTIO, Chile), using the 0.9-m telescope (*R* filter), and the Pico dos Dias Observatory (Laboratório Nacional de Astrofísica – OPD/LNA, Brazil), with the 1.6-m (*H* filter) and IAG 0.6-m (*V*, *I* filters) telescopes during 2011.

	CCD		IR
	CTIO/0.9-m	LNA/0.6-m	LNA/1.6-m
Filters	*R*	*V*, *I*	*H*
λ_c [nm]	658	551,806	1630
FOV [arcmin^2]	9.3	11.3	4
Scale [arcsec pixel^{-1}]	0.42	0.666	0.25
Date	10/04/2011	9–10/07/2011	06/04/2011
Seeing (arcsec)	1.3	2.5,1.7	1.0

λ_c: central wavelength.

of $EM = 4.5 \times 10^{24}$ cm^{-5} and $n_e = 2.6 \times 10^3$ cm^{-3}, respectively, both values typical of compact H II regions.

Later, Tapia et al. (2014) re-studied this star formation region, presenting new deep near-infrared broad- and narrow-band imaging and low-resolution spectroscopic observations, along with *Herschel* and *Spitzer* data. They found that the associate stellar cluster has at least 264 members, with 25 per cent of them showing infrared excess, inside an area of radius of 40 arcsec (0.4 pc for a quoted distance of 2 kpc), with the stellar population age ranging from 0.5–1.0 Myr, a result obtained from the use of isochrone fittings to the probable cluster members in the K_s versus $H - K_s$ diagram).

In this article, we present the first polarimetric study made in the direction of the RCW121 star formation region. It is part of a project aimed at performing multiband polarimetric observations in a large sample of Galactic star-forming regions (Santos, Roman-Lopes & Franco 2012; Santos et al. 2014).

The main goals were to derive the magnetic field orientation traced by the polarization vectors and to study the wavelength dependence of the polarization degree (using Serkowski's law) to derive the total-to-selective extinction ratio (R_V) distribution and the associated mean value, which relates to dust-grain properties.

2 OBSERVATIONS AND DATA REDUCTION

The polarimetric data used in this work were collected at Cerro Tololo InterAmerican Observatory (CTIO, Chile), using the 0.9-m telescope, and at the Pico dos Dias Observatory (Laboratório Nacional de Astrofísica – OPD/LNA, Brazil), using the 1.6-m and IAG (Instituto de Astronomía, Geofísica e Ciências Atmosféricas) 0.6-m telescopes during 2011. In Table 1, we present a journal of the observing runs and data set used in this work.

Both polarimeters used during the observing runs are able to measure linear polarization. They are of similar design, consisting of ensembles of optical and mechanical elements: a half-wave plate, a fixed analyser and a filter wheel. The half-wave plate is a crystal retarder placed at an angle ψ with respect to the North Celestial Pole (NCP). Its effect is to retard the light by means of a phase difference between parallel and perpendicular components of the electric field. It rotates by angles of 22.5°, therefore a polarization modulation cycle is completed for each 90° rotation. The analyser is a Savart plate that divides the light into two beams. Details of the instrument design are presented in Magalhães et al. (1996). Having the two beams present simultaneously represents an advantage, as this allows one to observe even under non-photometric conditions, as well as with the sky polarization being automatically cancelled during the reduction process (Carleton 1976).

Table 2. Polarimetric standards: literature values used in this work.

Polarized					
STD	Filter	*P* (per cent)	σ (per cent)	θ(°)	Ref
HD111579	*V*	6.460	0.014	103.11	(1)
	R	6.210	0.013	102.47	(1)
	I	5.590	0.017	102.00	(1)
	H	2.14	–	–	(1)
HD126593	*R*	4.821	0.012	74.81	(1)
HD110984	*V*	5.70	0.007	91.6	(1)
	I	5.167	0.007	90.82	(1)
HD170938	*V*	3.69	0.20	119.0	(2)
HD210121	*V*	1.21	0.05	154	(3)
HD164740	*H*	2.51	0.17	97	(4)
Unpolarized					
STD	Filter	*Q* (per cent)	*U* (per cent)	Ref	
HD150474	*R*	0.001	−0.007	(5)	
HD10038	*V*	0.11	−0.03	(6)	

The references correspond to (1) Turnshek et al. (1990), (2) Heiles (2000), (3) Larson, Whittet & Hough (1996), (4) Wilking, Lebofsky & Rieke (1982), (5) Gil-Hutton & Benavidez (2003), (6) Fossati et al. (2007),

2.1 Data reduction and polarimetric parameters of sources in RCW121

Data reduction and photometric measurements on the images were done using IRAF[1] tasks, with the point sources being identified and selected with the DAOFIND task, adopting a threshold value corresponding to the 5σ level above the local background and maximum data values below the saturation limits of the detectors. Photometry was performed on the images using the PHOT task, using 10 different apertures for each point source.

The polarization parameters were determined for each selected source using the PCCDPACK package[2] (Pereyra 2000), which consists of a set of IRAF routines and FORTRAN codes. It makes use of least-squares fit solutions of the modulation curves ($\cos 4\psi_i$, where ψ_i is the wave-plate position angle) to determine the normalized Stokes's parameters q and u ($q = Q/I$, $u = U/I$, where I is the Stokes parameter of light intensity and Q, U the Stokes's parameters of linear polarization). Then the polarization degree P and angle θ (measured from the North Celestial Pole to the east) are obtained from the well-known relations

$$P = \sqrt{q^2 + u^2} \qquad \text{and} \qquad \theta = (1/2)\arctan(u/q).$$

The errors associated with the polarization degree values (σ) are computed by PCCDPACK considering the error of the fitting process (Magalhães, Benedetti & Roland 1984), as well as the theoretical error from photon noise; in order to be conservative, we adopted the larger values out of both, which in general are obtained from the former. Additionally, since polarization degree is defined as a positive quantity, obtained from the Stokes parameters q and u through the equations above, the noise of these when squaring always contributes in a positive way, so its value is usually overestimated; this corresponds to a bias when measuring P. We have debiased it using the relation $P \rightarrow \sqrt{P^2 - \sigma^2}$, as suggested by Wardle & Kronberg (1974).

Polarimetric standards were observed each night (details are shown in Table 2) and unpolarized stars were used to determine the

[1] IRAF is distributed by the National Optical Astronomy Observatories, which are operated by the Association of Universities for Research in Astronomy, Inc., under cooperative agreement with the National Science Foundation.
[2] http://www.astro.iag.usp.br/~polarimetria/gaveta/reduc_detalhada.htm

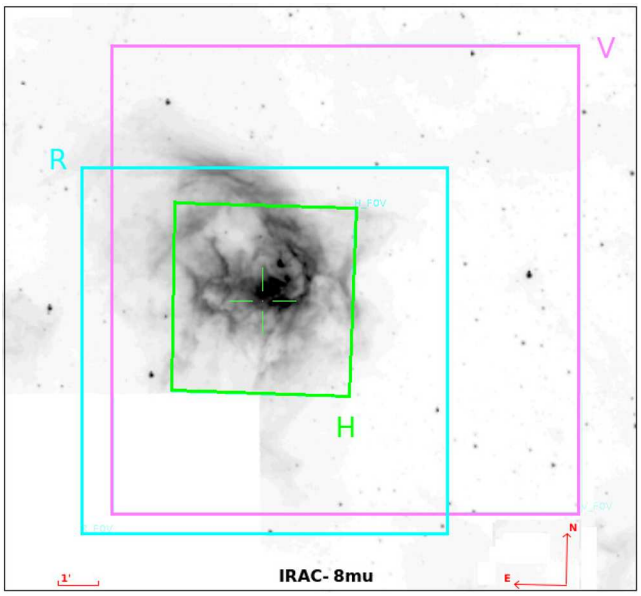

Figure 1. Field of view of *V*, *I* (identical), *R* and *H* bands overplotted on the *Spitzer* 8-μm image of RCW121.

instrumental polarization contribution, which in general has values of the order of ∼0.01 per cent, much less than the sensitivity reached with the instrument set-up used in our observations (typically errors of ∼0.05 per cent for stars with high signal-to-noise ratio). Polarized standard stars were used to set the zero-point of the polarization angles (see references in Table 2). Finally, the errors in the polarization angles ($e\theta$) were determined from $e\theta = 28.65^{\circ}(\sigma/P)$ for $P \gg \sigma$ (Serkowski 1958, 1962). In our analysis, we only consider polarization values with $P/\sigma > 3$, as this removes objects that are too faint, unpolarized and/or contaminated by cosmic rays and bad pixels. A sample of the catalogue for stars observed in the four bands is shown in Table A1; the complete catalogue will be available at http://vizier.u-strasbg.fr.

Fig. 1 shows the IRAC 8-μm image of RCW121 taken from the *Spitzer* archive, with the field of view of each filter indicated by the coloured squares. The filamentary structure of the dust cloud is quite visible, mainly in the darker part in the upper right corner of the region.

3 ANALYSIS AND RESULTS

3.1 Observed distribution of polarization angles

In general, the mean polarization angles obtained for each star in all bands present agreeable values (within errors). As the *R* band is the one that presents the largest number of sources with $P/\sigma > 3$, in Fig. 2 we show the corresponding polarization map, where we can see that the observed polarization angles are approximately aligned in the north–south direction. From the observed *R*-band FOV, we selected three subregions that present distinct characteristics. In Fig. 3, we show histograms of polarization. The histogram corresponding to area A (consisting mostly of the star-forming region, as indicated by the red rectangle – upper center position) presents a broad distribution of position angles, with many different orientations, and from the corresponding Gaussian fit we found $\theta = 16^{\circ} \pm 17^{\circ}$. On the other hand, the polarization angle distribution for sources in area B (delineated by the green rectangle – bottom left) constitutes a highly coherent sample with a narrow peak at $\theta = 5^{\circ} \pm 11^{\circ}$.

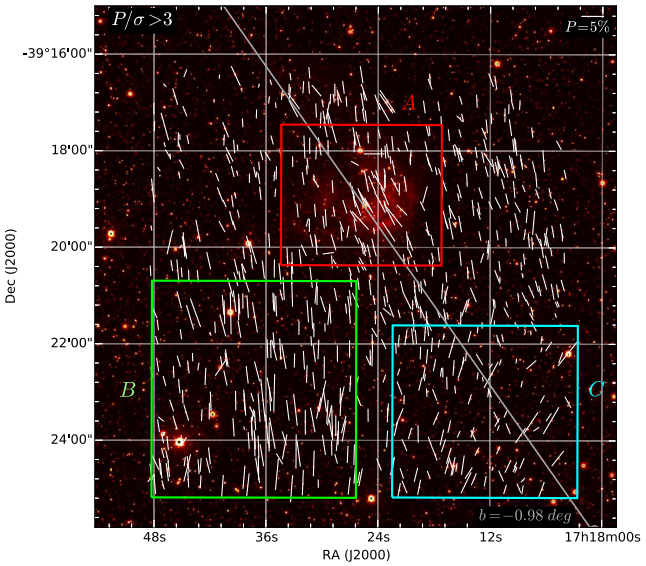

Figure 2. Polarization map for the *R* band, considering only data with $P/\sigma > 3$, with the scale for the polarization degree shown in the upper right corner. It seems that the polarization vectors align with distortions that can be related to the cloud structure. The dark grey diagonal line shows the Galactic parallel $b = -0.98^{\circ}$.

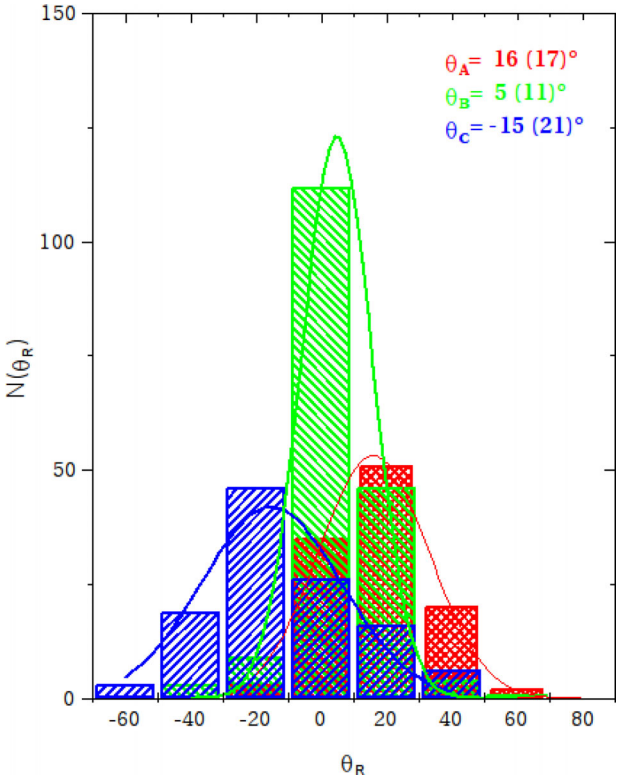

Figure 3. Distribution of polarization angle for three subregions, shown in Fig. 2. The red histogram corresponding to area A (containing mostly the star-forming region, as indicated by the red rectangle) presents a broad distribution of position angles. On the other hand, the polarization angles computed for sources in area B (green histogram, delineated by the green rectangle) constitute a highly coherent sample with a narrow peak on the observed distribution of polarization angles. Finally, the distribution of polarization angles from sources in area C (located to the southwest and delineated by the blue rectangle), represented by the blue histogram, mostly presents negative values.

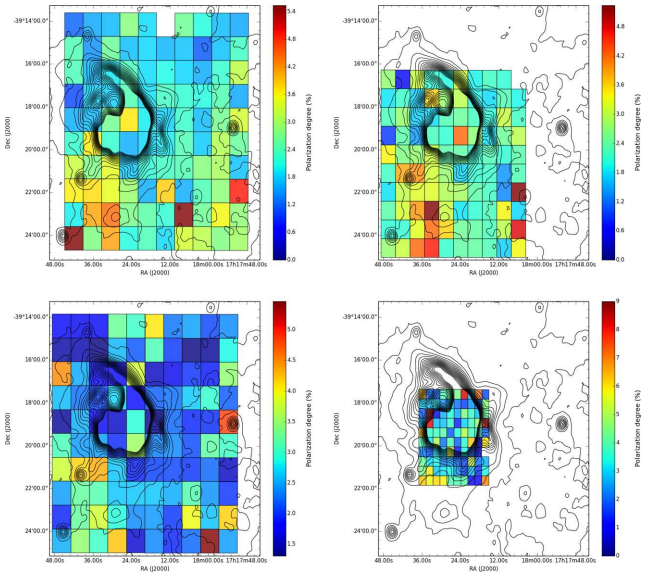

Figure 4. Polarization maps per bin for *V* (top left), *R* (top right), *I* (bottom left) and *H* (bottom right) filters (10 × 10 bins). The square bin sizes are approximately 1.11, 0.87, 1.12 and 0.43 arcmin for *V*, *R*, *I* and *H*, respectively. Contour plots are from the MSX 8.28-μm images.

Finally, the distribution of polarization angles from sources in area C (located to the southwest and delineated by the cyan rectangle) mostly presents negative values and has a mean position value of $\theta = -15^\circ \pm 21^\circ$.

3.2 Spatial distribution of polarization degree and angle

We studied the observed spatial distribution of polarization degree values from maps in RA and Dec. by deriving the mean of the observed polarization degree values (weighted by the associated errors) for all stars found inside the associated RA×Dec. bins. In order to obtain the best statistic per bin without losing spatial information, we used bin sizes optimized from the use of bidimensional maps obtained by maximizing the product of the number of stars per area times the number of bins. Finally, and in order to avoid outliers that could contaminate and distort the true mean values, we only used individual measurements within 3σ with respect to the mean.

From the polarization degree values, we constructed spatial maps of 10×10 square bins, while for the orientation vectors the maps are of 35×35 square bins. The polarization degree maps are shown in Fig. 4 and we can see that the mean polarization degree increases towards the south, perhaps because the dust column density is larger there, or maybe the orientation of field lines is better aligned with the sky in this particular area. On the other hand, the orientation of the lines tends to follow the cloud structure. Its elongated shape may be due to the magnetic pressure that opposes the H II expansion, which would be greater in the perpendicular direction to the magnetic field lines. The southwest area displays a different orientation, probably due to a difference in components in the line of sight.

Considering that the observed polarization angle for a given star does not vary much with the use of different filters, we also derived a master orientation map. For each star with polarimetric measurements in more than one band, we computed the associated weighted mean and, by following the procedure discussed above, a map was built; the result is shown in Fig. 5. There we can see that the orientation of the vectors in the inner parts of the region tends to follow the

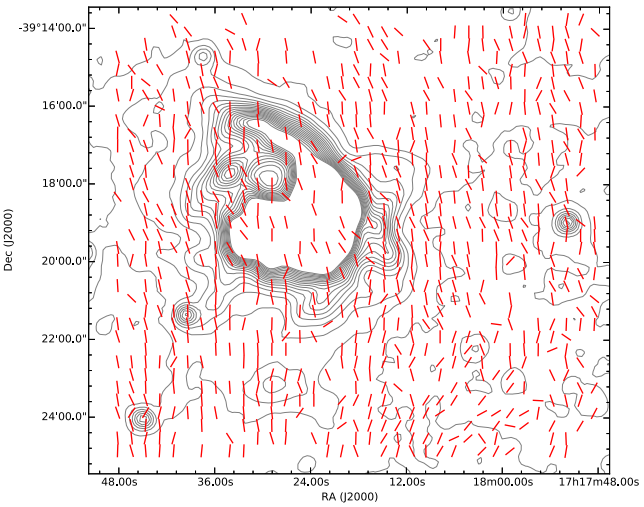

Figure 5. Orientation map from average polarization angle in RA–Dec. bins (35×35 bins) from the data available in the *VRIH* sample. The square bin size is approximately 0.33 arcmin. The contour map is from the MSX 8.28-μm image (north is up, east is left). The orientation of the lines tends to follow the cloud structure. Its elongated shape may be due to the magnetic pressure that opposes the H II expansion, which would be greater in the perpendicular direction to the magnetic field lines. The southwest area displays a different orientation, probably due to a difference in components in the light of sight.

shape of the H II region (projected on to the sky plane), following the behaviour predicted by the simulations of expanding H II regions discussed by Arthur et al. (2011).

3.3 Wavelength dependence of polarization degree and total-to-selective extinction ratio

Multiband polarimetric data allow us to study the wavelength dependence of the polarization degree, the total to selective extinction ratio and the grain size distribution using Serkowski's relation (Serkowski et al. 1975), which can be expressed as

$$\frac{P_\lambda}{P_{\max}} = \exp\left[-K\ \ln^2\left(\frac{\lambda_{\max}}{\lambda}\right)\right], \quad (1)$$

where P_λ is the polarization degree for a wavelength λ, $P_{\max}$ is the maximum polarization degree obtained from the fit to the data and $\lambda_{\max}$ is the corresponding wavelength for $P_{\max}$. K is a measure of the sharpness of the curve and there is evidence that this parameter may be a function of $\lambda_{\max}$ (e.g. Codina-Landaberry & Magalhaes 1976); however, we adopted the typically assumed value $K \cong 1.15$ (Serkowski et al. 1975), which is a good approximation, since our data do not present enough accuracy to allow setting K as a free parameter without introducing unnecessary noise to our analysis. Nonetheless, we performed a test setting K as a free parameter in the fit for our data points in the four bands; the difference in the parameter output ($P_{\max}$, $\lambda_{\max}$, subsequently R_V) is within its associated errors.

We computed fits of Serkowski's relation to the multiband data in our sample, considering the filter combinations *VRIH* (29 sources), *VRI* (168), *RIH* (47) and *VRH* (32). The *VIH* combination was not used in this analysis, because we wanted to use only combinations containing the *R*-band observations, as its data set in general present the smallest errors. The fitting was performed using the program EMCEE, a variant of Markov Chain Monte Carlo code (Foreman-Mackey et al. 2013). Fig. 6 shows two examples of Serkowski's relation fitted to two stars with $P/\sigma > 3$ in the *VRIH* bands.

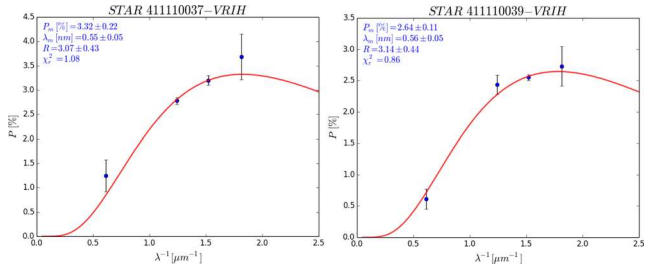

Figure 6. Diagrams of P–λ^{-1} and fits of Serkowski's relation for two objects present in four bands towards RCW121. The values of $P_{\max}$, $\lambda_{\max}$ and R_V determined are shown in the upper left corner.

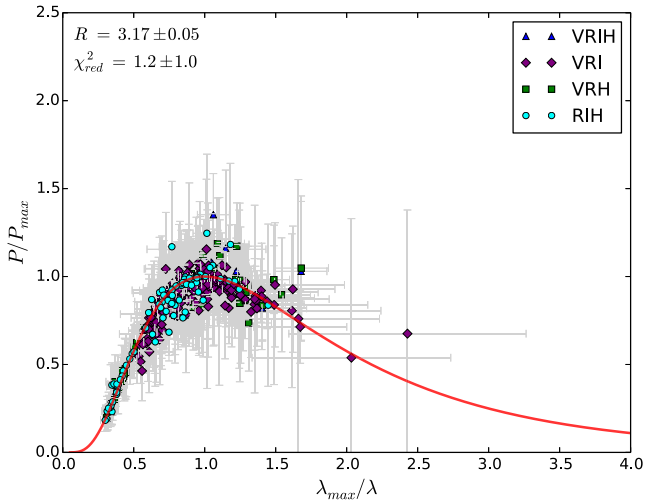

Figure 7. Diagram of $P/P_{\max}$ for all combinations used: *VRIH* (blue triangles), *VRI* (purple diamonds), *VRH* (green squares) and *RIH* (cyan circles). The red curve shown in this figure represents Serkowski's relation associated with the final R_V weighted averaged value computed from the entire sample (and not from a fitting to the observed distribution). Error bars are shown in grey. Central wavelengths are given in Table 1.

The individual values of the total-to-selective extinction ratio R_V (defined as $A_V/E(B-V)$) for each of our 103 stars (with good chi-squared reduced values and low individual errors) were computed using the relation $R_V = (5.6 \pm 0.3)\lambda_{\max}$ (Whittet & van Breda 1978). The final R_V weighted averaged value obtained from the entire sample is $R_V = 3.17 \pm 0.05$ – a result slightly above but not so different from the Galactic canonical value $R_V \approx 3.09 \pm 0.03$ (Rieke & Lebofsky 1985). In Fig. 7, we introduce the master $[(P/P_{\max}) \times (\lambda_{\max}/\lambda)]$ diagram, where we present the points obtained from all combinations mentioned above. We can see that most of the points are distributed along a band towards the Serkowski's relation associated with the obtained weighted average value of $R_V = 3.17 \pm 0.05$.

The observed distribution of R_V values is shown in Fig. 8; this presents a peak for values around the one obtained for the Galactic normal interstellar medium, with a tail towards larger R_V values. In Fig. 9 we also present the mean values of R_V in a RA and Dec. spatial map. We did this by computing the mean values of R_V for the stars in each RA–Dec. bin, together with the MSX 8.28-μm contour plot. We can see that most of the R_V values in the range $2.5 \lesssim R_V \lesssim 3.5$ are found in the inner parts of RCW121 (close to the compact H II region), with the higher R_V values preferentially located in the borders of the RCW121 region. High R_V values can be attributed to dense regions, where dust grains are supposedly larger.

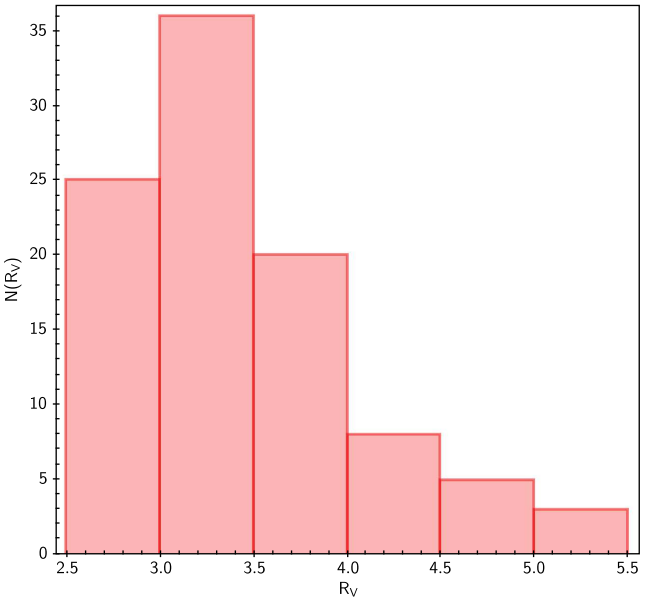

Figure 8. Observed distribution of total-to-selective extinction (R_V) values in the direction of RCW121.

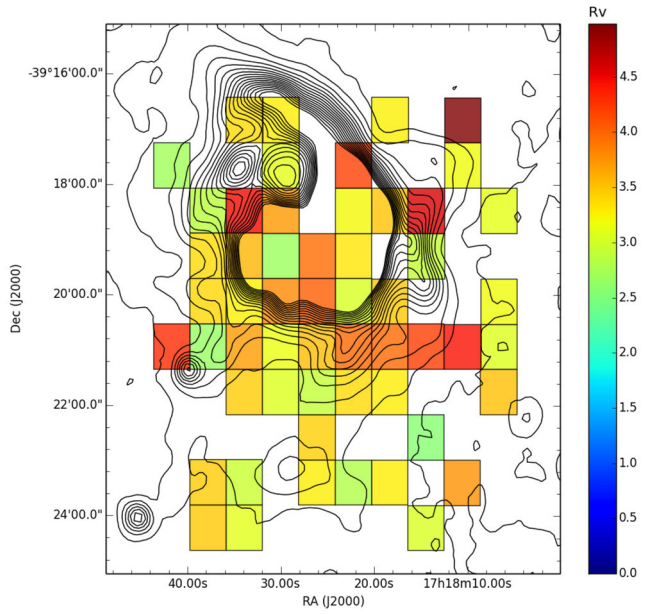

Figure 9. Total-to-selective extinction ratio map by spatial bins. Each coloured bin contain a minimum of one star (with an average of 1.35 sources per bin). The square bin size is 0.8 arcminu. The contour corresponds to the MSX 8.28-μm image (north is up, east is left).

3.4 Foreground *R*-band polarization component

Polarization measurements of sources towards the region under study are affected by a foreground component in the direction of the cloud that hosts RCW121. Therefore, in order to subtract this component from the results, it is necessary to quantify it properly. Stellar groups can be separate in different ways, for example Martínez, Vergne & Feinstein (2004) used the distribution of polarization position angle to distinguish between Hogg 22 and NGC 5204 open cluster stars, which show different mean polarization angles. In the case of having foreground sources at different distances, photometry is introduced: the colour distribution and its relation to polarization

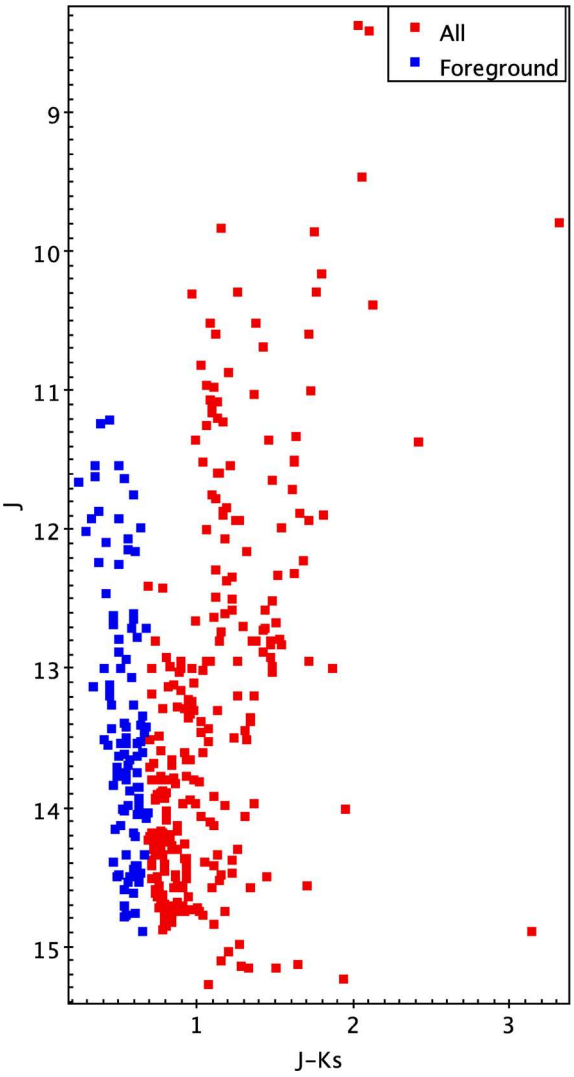

Figure 10. (J versus $J - K_S$) colour–magnitude diagram (CMD) of sources in the direction of RCW121. The blue vertical sequence seen in this diagram is populated mainly by main-sequence foreground disc stars.

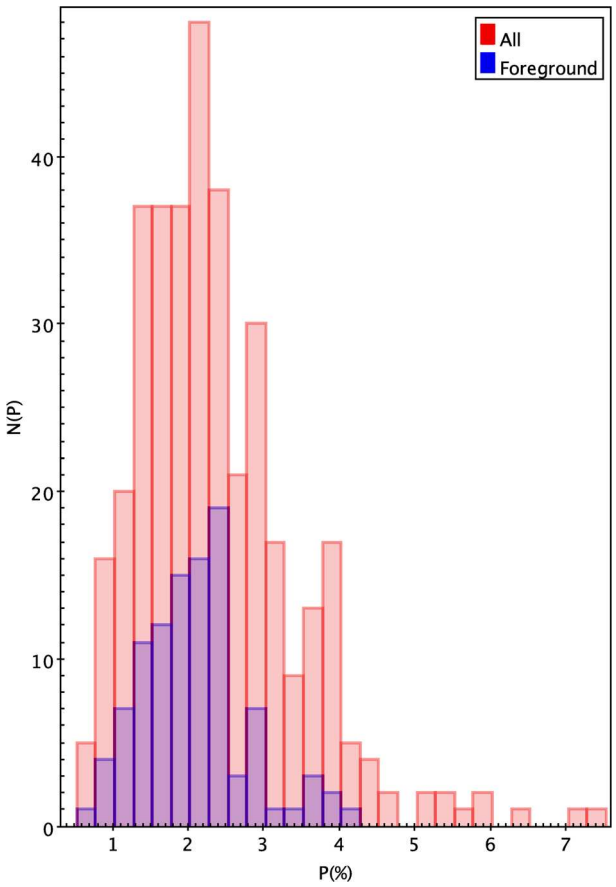

Figure 11. Histogram of polarization degree values for all sources (in red) with good polarimetric measurements in the R-band field of view, together with a second histogram built with sources restricted to the (blue) vertical foreground sequence seen in the CMD (Fig. 10). While the former presents an approximate Gaussian distribution, the histogram made from the restricted sample shows a different form. Indeed, in this case $N(P)$ grows with P until reaching $P \approx 2.5$ per cent, dropping suddenly after this value. We interpret this brake on the observed distribution as corresponding to the maximum value of P generated by the intervening ISM between the observer and the RCW121 molecular cloud region.

degree and angle can be used to separate these groups (e.g Santos et al. (2014)). We investigated the colours and related polarization degree values of stars in the direction of RCW121. We did this for all sources in the Two Micron All-Sky Survey (2MASS) Point Source Catalog (PSC) found in the R-band field of view, presenting magnitude errors smaller than 0.15 mag in the J, H and K_S bands. In Fig. 10, we show the (J versus $J - K_S$) colour–magnitude diagram (CMD) obtained from the 2MASS point sources found in the area studied. There we can see the vertical blue sequence of low-reddened stars that belong mainly to main-sequence Galactic disc population. Moreover, in Fig. 11 we present the histogram of polarization degree values for all sources (in red) with good polarimetric measurements in the associated field of view, together with a second histogram constructed with sources restricted to the (blue) vertical foreground sequence seen in Fig. 10. While the former presents an approximate Gaussian distribution for the observed P values, the histogram made from the restricted sample shows a different form. Indeed, in this case $N(P)$ grows with P until $P \approx$ 2.5 per cent is reached, dropping suddenly after this value. We interpret this brake on the observed distribution as corresponding to the maximum value of P generated by the intervening ISM between the observer and the RCW121 molecular cloud region. In order to verify the consistency of this result, we also obtained another estimate for the maximum value for the foreground component by analysing the results obtained in a control field. From a theoretical point of view, an ideal control area would be one that enables us to derive the foreground component of the polarization without the effects generated by the presence of the molecular cloud associated with RCW121. As mentioned before, in Fig. 5 the 8-μm *Spitzer* contour plot in the direction of RCW121 is shown. It can be seen there that the southwest region is apparently free of dust emission, suggesting that the associated line of sight could be used as a control field. Therefore we studied the polarization degree distribution (shown in the right panel of Fig. 12), which for the foreground control component (selected from the CMD diagram presented in the left panel of 12) has a peak at ∼2.0–2.5 per cent, a value consistent with that determined from the foreground sources found in the previous paragraph (Figure 11). Indeed, both results are consistent with the polarization degree values (between ∼1.5 and 2.5) of field stars towards the direction of RCW121 and at its distance published by Heiles (2000). Also, the mean polarization angle can be estimated

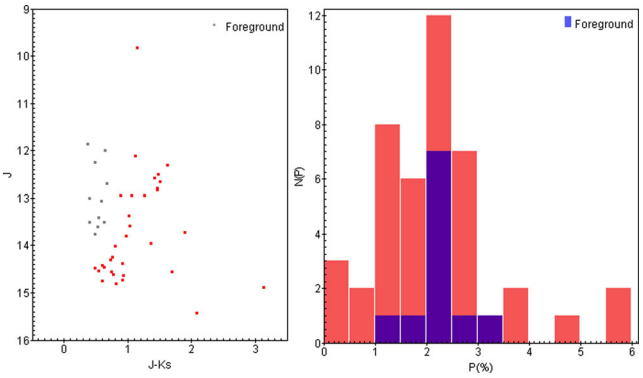

Figure 12. *Left:* colour–magnitude diagram for sources in the control area, with the foreground stars indicated in blue (to the upper left group). *Right:* histograms of the polarization angle of sources in the control area, with the distribution from foreground sources corresponding to the blue one.

from the observed distribution in area C (shown in Fig. 3), which peaks at $\theta \sim -25^{\circ}$. Therefore this is the value of $\theta_{\rm f}$ associated with the polarization angle of the foreground component that is used to correct our results from this component.

In order to remove the foreground component from each star with good polarization values in the *R*-band polarimetric catalogue associated with the RCW121 cloud, we applied the Stokes' parameters superposition principle, in which the measured q and u values must be equal to the foreground component ($q_{\rm F}$ and $u_{\rm F}$) obtained from the known relations $q = P\cos(2\theta)$ and $u = P\sin(2\theta)$, $q_{\rm F} = -0.011$ and $u_{\rm F} = 0.017$, plus the parameters associated with RCW121 ($q_{\rm RCW121}$ and $u_{\rm RCW121}$):

$$\begin{aligned} q &= q_{\rm F} + q_{\rm RCW121}, \\ u &= u_{\rm F} + u_{\rm RCW121}. \end{aligned} \quad (2)$$

This procedure was applied to selected sources associated with the cloud–H II region area. A total of 19 stars (with good polarimetric values in the *R* band and in the 2MASS catalogue) classified as background sources plus 39 stars identified as cluster candidates from Roman-Lopes & Abraham (2006) and 38 stars present in Tapia et al. (2014), with 14 sources repeated in the last 2 catalogues, were used; the results are shown in Fig. 13. There we can see the polarization map from the sources in the direction of RCW121, already corrected for the contribution of the foreground component. The main tendency of the orientation of the polarization angles remains approximately the same, preferentially aligned close to the north–south direction, with a slight tendency to deviate in the inner parts of the H II region. The position angle distribution for these sources obtained from a Gaussian fit is $-12^{\circ} \pm 7^{\circ}$; this value represents the mean value for the orientation of the sky-projected magnetic field associated with RCW121.

Fig. 13 also shows three dense cores identified by Tapia et al. (2014) as young stellar objects, core I being the youngest undetected at $\lambda < 100\,\mu$m, while cores II and III are more evolved and have NIR counterparts. None of these has a match in our polarimetric catalogue, nor do we see a different trend around them, but our resolution is not as deep; for the same reason, other sources identified as having NIR excess (in table 5 and figs 13 and 15 of Tapia et al. 2014) are not present in our data either, with the exception of B2, identified as 401001917, which has a decontaminated polarization degree in the *R* band of 2.4 per cent and position angle 18°, values that fall within the overall distribution. Objects with characteristic pre-main sequence colours also have values within

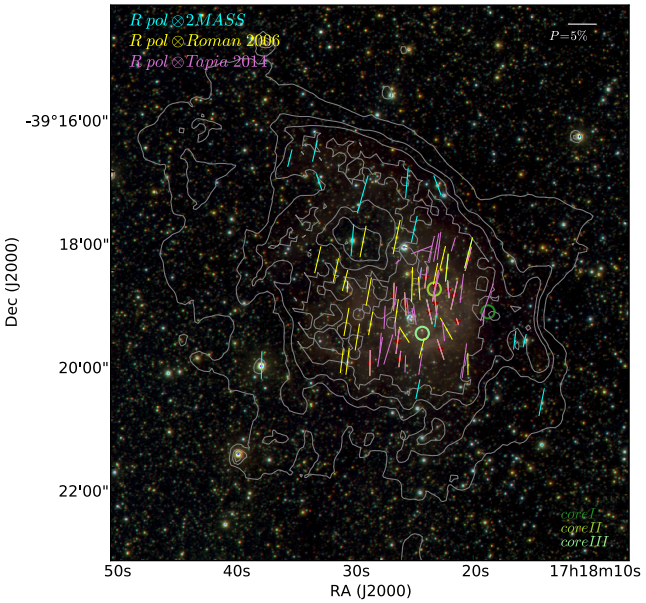

Figure 13. Polarization map of sources associated with RCW121 corrected from the foreground component. The cyan lines correspond to the polarization vectors of sources in the *R*-band polarimetric catalogue, restricted to the science area and fulfilling the background colour criteria (19 stars). Yellow lines correspond to sources presented in the catalogue for stellar cluster candidates of Roman-Lopes & Abraham (2006) (37 stars) and orchid lines belong to sources in Tapia et al. (2014) (38 stars), of which 14 sources overlap with the Roman-Lopes & Abraham (2006) catalogue, marked with dark red star symbols. The three cores identified as young stellar objects by Tapia et al. (2014) are shown in green, as described by the bottom right caption legend. The orientation shows a tendency close to north–south, with some deviations that can be related to the cloud structure. Contours are from the *Spitzer* 8-μm image. The background colour image is from *JHK* bands from the *VVV* survey. North is up and east left.

the general distributions of P and θ, therefore we did not detect intrinsic polarization. The presence of near-infrared excess does not necessarily imply measurable levels of intrinsic polarization. In general, intrinsic polarization levels due to radiation scattering by dust in a circumstellar disc depend on several factors, such as how evolved the disc is (density and structure), its inclination relative to the line of sight and its distribution of grain sizes. In this case, it is clear from the comparison of polarization degree and the angle between sources with near-infrared excess and surrounding objects that, even if some intrinsic polarization is present, the interstellar component is probably dominant.

4 CONCLUSIONS

In this work, we performed a polarimetric study of the RCW121 star-forming region. We derived the magnetic field orientation traced by the polarization vectors, obtaining the polarization component associated with RCW121 (corrected from the associated maximum foreground component), and also studied the wavelength dependence of the polarization degree (using Serkowski's relation) to derive the total-to-selective extinction ratio (R_V) distribution and associated mean value. The main results obtained are as follows.

(i) In general, the mean polarization angles obtained for each star in all bands present agreeable values within the quoted errors. From the statistical study of position-angle values in the direction

of the RCW121 H II region, a broad distribution with many different orientations was found.

(ii) From the study of the observed spatial distribution of polarization degree and angle values, we found that the mean polarization degree increases towards the south, perhaps because the dust column density is larger there or maybe the magnetic field lines are better aligned with the sky in this particular area. On the other hand, the orientation of the lines tends to follow the cloud elongated structure; this shape is perhaps due to the magnetic pressure that opposes H II region expansion, which would be greater in the perpendicular direction to the magnetic field lines. Indeed, for each star with polarimetric measurements in more than one band, we computed the associated weighted mean, concluding that the orientation of the vectors in the inner parts of the region tends to follow the shape of the H II region (projected on to the sky plane), following the behaviour predicted by the simulations of expanding H II regions discussed by Arthur et al. (2011).

(iii) From the individual values of total-to-selective extinction ratio R_V, for 103 stars (with good chi-squared reduced values), we derived the final R_V weighted averaged value in the direction of RCW121 as $R_V = 3.17 \pm 0.05$, a result slightly above but not so different from the Galactic canonical value $R_V \sim 3.09 \pm 0.03$ (Rieke & Lebofsky 1985).

(iv) We derived the foreground component of the polarization degree from the study of associated values from field stars towards the RCW121 region and found that it corresponds to ∼2.0–2.5 per cent, a result consistent with that found by Heiles (2000). We determined the orientation of the sky-projected magnetic field associated with RCW121 (shown in Fig. 13); the mean value is $-12^\circ \pm 7^\circ$, obtained from a Gaussian fit to the distribution of position-angle values.

ACKNOWLEDGEMENTS

We are grateful to the anonymous referee for very valuable suggestions and comments. We thank the staff of the CTIO (Chile) and OPD/LNA (Brazil) for their hospitality and invaluable help during our observing runs. GAPF acknowledges the Brazilian agencies FAPEMIG and CNPq. ARL acknowledges partial support from DIULS regular project PR15143. JCSN thanks Dr Carlos Contreras for introducing EMCEE and for his constant support.

This article is based on observations obtained at the Cerro Tololo InterAmerican Observatory (CTIO – Chile) and at Observatório do Pico dos Dias (OPD–Brazil).

This research has made use of the VizieR catalogue access tool, CDS, Strasbourg, France. The original description of the VizieR service was published in Ochsenbein, Bauer & Marcout (2000).

REFERENCES

Andersson B.-G., Lazarian A., Vaillancourt J. E., 2015, ARA&R, 53, 501
Arnal E. M., Duronea N. U., Testori J. C., 2009, in Rev. Mex. Astron. Astrofis. Conf. Ser., 35, 48
Arthur S. J., Henney W.-J., Mellema G., de Colle F., Vasquez-Semadeni E., 2011, MNRAS, 414, 1747
Bronfman L., Nyman L.-A., May J., 1996, A&AS, 115, 81
Carleton N., 1976, Methods of Experimental Physics Vol. 12, Astrophysics. Part A: Optical and Infrared. Academic Press, New York, NY
Codina-Landaberry S., Magalhaes A. M., 1976, A&A, 49, 407
Dolginov A. Z., Mytrophanov I. G., 1976, Ap&SS, 43, 257
Foreman-Mackey D., Hogg D. W., Lang D., Goodman J., 2013, PASP, 125, 306
Fossati L., Bagnulo S., Mason E., Landi Degl'Innocenti E., 2007, in Sterken C., ed., ASP Conf. Ser. Vol. 364, The Future of Photometric, Spectrophotometric and Polarimetric Standardization. Astron. Soc. Pac., San Francisco, p. 503
Gil-Hutton R., Benavidez P., 2003, MNRAS, 345, 97
Heiles C., 2000, AJ, 119, 923
Larson K. A., Whittet D. C. B., Hough J. H., 1996, ApJ, 472, 755
Magalhães A. M., Benedetti E., Roland E. H., 1984, PASP, 96, 383
Magalhães A. M., Rodrigues C. V., Margoniner V. E., Pereyra A., Heathcote S., 1996, in Roberge W. G., Whittet D. C. B., eds, ASP Conf. Ser. Vol. 97, Polarimetry of the Interstellar Medium. Astron. Soc. Pac., San Francisco, p. 118
Martínez R., Vergne M. M., Feinstein C., 2004, A&A, 419, 965
McKee C. F., Ostriker E. C., 2007, ARA&A, 45, 565
Ochsenbein F., Bauer P., Marcout J., 2000, A&AS, 143, 23
Pereyra A., 2000, PhD thesis, Universidade de Sâo Paulo, Brazil
Rieke G. H., Lebofsky M. J., 1985, ApJ, 288, 618
Rodgers A., Campbell C. T., Whiteoak J. B., 1960, MNRAS, 121, 103
Roman-Lopes A., Abraham Z., 2006, AJ, 131, 951
Sánchez-Monge Á., Beltrán M. T., Cesaroni R., Fontani F., Brand J., Molinari S., Testi L., Burton M., 2013, A&A, 550, A21
Santos F. P., Roman-Lopes A., Franco G. A. P., 2012, ApJ, 751, 138
Santos F. P., Franco G. A. P., Roman-Lopes A., Reis W., Román-Zúñiga C. G., 2014, ApJ, 783, 1
Serkowski K., 1958, Acta Astron., 8, 135
Serkowski K., 1962, in Kopal Z., ed., Advances on Astronomy and Astrophysics. Academic Press, p. 289
Serkowski K., Mathewson D. S., Ford V. L., 1975, ApJ, 196, 261
Sharpless S., 1959, ApJS, 4, 257
Tapia M., Persi P., Roth M., Elia D., Molinari S., Saldaño H. P., Gomez M., 2014, MNRAS, 437, 606
Turnshek D. A., Bohlin R. C., Williamson R. L., II, Lupie O. L., Koornneef J., Morgan D. H., 1990, AJ, 99, 1243
Walsh A. J., Hyland A. R., Robinson G., Burton M. G., 1997, MNRAS, 291, 261
Wardle J. F. C., Kronberg P. P., 1974, ApJ, 194, 249
Whittet D. C. B., van Breda I. G., 1978, A&A, 66, 57
Wilking B. A., Lebofsky M. J., Rieke G. H., 1982, AJ, 87, 695

SUPPORTING INFORMATION

Additional Supporting Information may be found in the online version of this article:

(http://www.mnras.oxfordjournals.org/lookup/suppl/doi:10.1093/mnras/stw1666/-/DC1).

Please note: Oxford University Press is not responsible for the content or functionality of any supporting materials supplied by the authors. Any queries (other than missing material) should be directed to the corresponding author for the article.

APPENDIX A: TABLES

The catalogue for stars in all bands (*V*, *R*, *I*, *H*) is presented in Table A1.

Table A1. Catalogue of the stars present in all bands (*VRIH*) with $P/\sigma > 3$. The first column is the unique index given to each star, columns 2 and 3 are right ascension and declination (J2000), columns 4, 6, 8 and 10 are the polarization degree with its error in parentheses and columns 5, 7, 9 and 11 are the polarization angle with its error, for *V*, *R*, *I* and *H* bands, respectively.

Index	RA (deg)	Dec. (deg)	P_V (σ_V) (per cent)	θ_V ($e\theta_V$) (°)	P_R (σ_R) (per cent)	θ_R ($e\theta_R$) (°)	P_I (σ_I) (per cent)	θ_I($e\theta_I$) (°)	P_H (σ_H) (per cent)	θ_H($e\theta_H$) (°)
411110010	259.6459	−39.3145	1.80(0.52)	3.3(8.2)	1.44(0.19)	− 7.3(3.7)	2.03(0.58)	11.2(8.1)	1.22(0.23)	− 3.2(5.5)
411110013	259.6432	−39.3498	1.45(0.19)	18.8(3.7)	1.96(0.06)	16.9(0.8)	1.36(0.25)	12.5(5.3)	0.75(0.15)	12.3(5.8)
411110017	259.6405	−39.3368	3.60(0.39)	0.4(3.1)	3.38(0.15)	3.1(1.3)	2.67(0.14)	3.4(1.6)	1.05(0.10)	8.8(2.8)
411110019	259.6383	−39.3388	3.49(0.20)	-2.7(1.6)	3.74(0.16)	3.3(1.2)	2.70(0.18)	2.1(1.9)	1.10(0.15)	6.8(4.0)
411110029	259.6299	−39.3437	3.36(0.63)	11.9(5.4)	3.64(0.22)	8.5(1.7)	3.49(0.80)	2.4(6.6)	0.97(0.29)	− 10.1(8.7)
411110032	259.6286	−39.3619	2.12(0.48)	12.7(6.5)	2.46(0.10)	0.8(1.1)	1.78(0.36)	13.4(5.8)	0.62(0.16)	− 5.5(7.3)
411110037	259.6261	−39.2985	3.69(0.47)	8.8(3.6)	3.20(0.10)	10.9(0.9)	2.78(0.07)	7.9(0.8)	1.25(0.33)	15.9(7.5)
411110039	259.6224	−39.2988	2.73(0.32)	-2.2(3.3)	2.55(0.05)	0.8(0.5)	2.43(0.15)	2.9(1.8)	0.61(0.16)	− 5.5(7.6)
411110042	259.6197	−39.3210	1.84(0.04)	9.9(0.7)	1.75(0.05)	12.1(0.8)	1.23(0.11)	11.4(2.6)	0.78(0.12)	18.4(4.5)
411110051	259.6088	−39.3460	2.07(0.26)	2.4(3.6)	2.08(0.16)	9.2(2.2)	1.56(0.21)	13.2(3.9)	0.91(0.12)	18.3(3.9)
411110053	259.6068	−39.3391	2.29(0.29)	31.3(3.7)	2.71(0.08)	33.9(0.8)	1.90(0.26)	35.7(3.9)	1.14(0.07)	39.7(1.8)
411110057	259.6034	−39.3436	1.59(0.42)	17.9(7.5)	0.95(0.11)	11.7(3.3)	1.54(0.14)	21.7(2.6)	0.52(0.10)	27.5(5.7)
411110059	259.6018	−39.3276	1.29(0.07)	9.8(1.5)	1.10(0.06)	11.6(1.6)	0.63(0.11)	4.5(4.9)	0.52(0.10)	19.3(5.2)
411110060	259.6018	−39.3515	1.61(0.07)	8.0(1.3)	1.69(0.01)	13.6(0.2)	1.32(0.21)	23.4(4.6)	0.61(0.06)	16.3(2.9)
411110064	259.5992	−39.3178	2.04(0.67)	35.0(9.5)	4.31(0.18)	34.0(1.2)	2.63(0.68)	33.5(7.4)	1.58(0.29)	30.7(5.3)
411110067	259.5971	−39.3520	1.35(0.18)	9.8(3.9)	1.85(0.07)	10.8(1.1)	2.14(0.51)	23.6(6.9)	0.65(0.07)	11.4(3.0)
411110068	259.5965	−39.3486	1.75(0.25)	12.9(4.2)	1.75(0.21)	11.8(3.4)	1.68(0.23)	8.0(3.9)	0.88(0.23)	12.8(7.6)
411110071	259.5953	−39.3280	3.83(0.77)	38.7(5.7)	4.36(0.21)	40.2(1.4)	4.17(0.51)	37.7(3.5)	0.91(0.23)	37.7(7.4)
411110075	259.5909	−39.2996	2.21(0.43)	23.3(5.6)	0.80(0.12)	38.8(4.5)	4.04(1.21)	45.8(8.6)	1.38(0.30)	13.2(6.2)
411110077	259.5906	−39.3133	2.65(0.36)	-7.8(3.9)	2.11(0.11)	− 0.9(1.5)	1.03(0.21)	− 38.7(5.9)	0.90(0.27)	8.2(8.5)
411110078	259.5884	−39.3378	2.57(0.26)	10.1(2.9)	2.17(0.06)	7.4(0.7)	1.85(0.31)	9.4(4.9)	0.60(0.08)	11.7(3.8)
411110082	259.5857	−39.3035	1.21(0.08)	4.9(2.0)	1.40(0.09)	1.1(1.9)	1.02(0.16)	5.7(4.4)	0.58(0.06)	3.2(2.9)
411110083	259.5846	−39.3532	1.63(0.10)	-0.9(1.8)	1.68(0.06)	− 1.0(1.0)	1.43(0.20)	4.1(4.1)	0.59(0.08)	9.7(3.8)
411110088	259.5831	−39.3522	2.27(0.30)	16.3(3.8)	2.08(0.17)	13.6(2.4)	5.92(0.86)	− 35.2(4.2)	1.39(0.20)	32.4(4.1)
411110094	259.5783	−39.3575	2.15(0.34)	4.9(4.6)	2.18(0.04)	3.6(0.5)	1.59(0.16)	7.1(2.9)	0.88(0.04)	8.8(1.4)
411110096	259.5779	−39.3030	2.82(0.45)	13.1(4.6)	2.33(0.08)	19.0(1.0)	1.27(0.34)	20.0(7.8)	1.12(0.29)	12.2(7.4)
411110102	259.5757	−39.3407	2.45(0.39)	-0.7(4.6)	2.57(0.10)	− 1.5(1.2)	2.38(0.18)	3.3(2.1)	0.88(0.05)	3.1(1.7)
411110103	259.5757	−39.3368	2.61(0.50)	27.9(5.5)	1.64(0.10)	14.1(1.7)	1.29(0.25)	21.3(5.6)	0.99(0.16)	23.0(4.7)
411110109	259.5705	−39.3038	2.49(0.31)	15.4(3.5)	1.80(0.04)	16.1(0.6)	1.62(0.10)	16.2(1.8)	0.70(0.16)	28.0(6.6)

This paper has been typeset from a TEX/LATEX file prepared by the author.